

Evaluation of the HOMME Dynamical Core in the Aqua-Planet Configuration of NCAR CAM4: Rainfall

Saroj K. Mishra^{1,2}, Mark A. Taylor³, Ramachandran D. Nair², Peter H. Lauritzen², Henry
M. Tufo^{1,2}, Joseph J. Tribbia²

¹Department of Computer Science, University of Colorado, Boulder, CO, USA

²National Center for Atmospheric Research (NCAR), Boulder, CO, USA

³Sandia National Laboratories, Albuquerque, NM, USA

Submitted to Journal of Climate: May-11-2010

Revised for Journal of Climate: December-15-2010

Corresponding Address: saroj@ucar.edu

Institute for Mathematics Applied to Geosciences (IMAGE)

[#]National Center for Atmospheric Research (NCAR)

Boulder, CO, 80305, USA.

Phone: 303-497-2486

Fax: 303-497-2483

[#]The National Center for Atmospheric Research is sponsored by the National Science Foundation

Abstract

The NCAR-Community Climate System Model version 4 (CCSM4) includes a new dynamical core option based on NCAR's High-Order Method Modeling Environment (HOMME). HOMME is a petascale capable high-order element-based conservative dynamical core developed on the cubed-sphere grid. Initial simulations have been completed in aqua-planet configuration of CAM4, the atmospheric component of CCSM4. We examined the results of this simulation and assessed its fidelity in simulating rainfall, which is one of the most important components of the Earth's climate system. For this we compared the results from two other dynamical cores of CAM4, the finite volume (FV) and Eulerian (EUL).

Instantaneous features of rainfall in HOMME are similar to FV and EUL. Similar to EUL and FV, HOMME simulates a single peak Inter Tropical Convergence Zone (ITCZ) over the equator. The strength of the ITCZ is found to be almost same in HOMME and EUL but more than that in FV. It is observed that in HOMME and EUL there is higher surface evaporation, which supplies more amount of moisture into the deep tropics and gives more rainfall over the ITCZ. The altitude of maximum precipitation is found to be at almost the same level in all the three dynamical cores. The eastward propagation of rainfall bands is organized in FV and HOMME, and more prominent than in EUL. The phase speed of the eastward propagation in HOMME is found to be higher than that in FV. Our results show that, in general, the rainfall simulated by HOMME falls in a regime between that of FV and EUL. Hence, we conclude that the key aspects of rainfall simulation with HOMME falls in an acceptable range, as compared to the existing dynamical cores used in the model.

1 Introduction

General circulation models (GCMs) are an effective tool to improve our understanding of the present and past climate as well to predict the future climate. The present day numerical models are yet to capitalize on the enormous computing power made available by petascale capable high performance computers. The GCMs broadly consist of two components, namely, the dynamical core and the physical parameterization suite. The dynamical core numerically solves the system of partial differential equations, which govern the fluid motion, while the physics package provides the numerous forcing terms used in these equations.

In order to take advantage of the high performance computing, improvement of the dynamical core used in the present day GCM is of paramount importance. Currently, most of the operational dynamical cores use latitude-longitude based grids. The grid lines cluster at the pole, creating a potentially severe CFL restriction on the time step. There are many successful techniques to handle this pole problem; however, most of them (e.g., polar filters) substantially degrade parallel scalability by limiting the model to one-dimensional domain decomposition strategies. However, future evolution of the Community Climate System Model (CCSM) into an Earth system model requires a highly scalable and accurate formulation of the dynamics of the atmosphere.

The High Order Method Modeling Environment (HOMME) is a highly scalable, global hydrostatic atmospheric modeling framework (Dennis et al., 2005; Nair 2007; Nair 2009). Recently, HOMME has been integrated into the Community Atmospheric Model (CAM), the atmospheric component of the CCSM. HOMME relies on a cubed-sphere grid, where the planet Earth is tiled with quasi-uniform quadrilateral elements, free from polar singularities. HOMME is the first dynamical core ever that allows for full two-dimensional

domain decomposition in CAM.

Recent performance comparisons of CAM-FV and CAM-HOMME (A. Mirin, personal communication, 2010) show that at the resolution used here, CAM-FV is twice as fast as CAM-HOMME on 32 processor cores of the JaguarPF Cray XT-5 at Oak Ridge National Laboratory. Due to CAM-HOMME's increased scalability, CAM-HOMME starts to outperform CAM-FV on 512 cores and higher. CAM-HOMME achieves a maximum integration rate of 82 simulated-years-per-day (SYPD) on 2700 cores, compared to CAM-FV's maximum of 50 SYPD on 3328 cores. At higher resolutions, the improvements due to increased scalability become larger. At 1/4 degree resolution, on the Intrapid BG/P system at Argonne National Laboratory, CAM-HOMME can achieve 12 SYPD on 86,400 cores, while CAM-FV achieves its maximum rate of 2.5 SYPD on 53248 cores (Edwards et al., 2011)

HOMME simulations presented in this paper use the physics package of CAM, version 4 (Neale et al., 2010) in the aqua-planet configuration. Since rainfall is one of the most important components of the Earth's climate system, its simulation is examined in this paper. Here the simulated rainfall from HOMME has been compared with FV and EUL dynamical cores.

The organization of the paper is as follows. Section 2 briefly outlines model details and section 3 describes the simulation details. Results are presented in section 4, followed by the summary and conclusions in section 5.

2 Brief Description of CAM4

The Community Atmosphere Model version 4 (CAM4) is the sixth generation of atmospheric general circulation models (AGCMs) developed by the atmospheric modeling

community in collaboration with the National Center for Atmospheric Research (NCAR). The source code, documentation and input datasets for the model are freely available from the CAM website (<http://www.cesm.ucar.edu/models/ccsm4.0/cam/>). Since a detail description of CAM4 is given in Neale et al. (2010), we will not discuss the details of model here. Nevertheless, certain aspects of the model, relevant to this work, are explained in the following.

CAM4 has been designed to produce simulations with reasonable accuracy for various dynamical cores and horizontal resolutions. For this study, FV, EUL, and HOMME dynamical cores were used at 1^0 equivalent resolutions in horizontal and 26 levels in the vertical. The model uses the hybrid vertical coordinate, which is terrain following at earth's surface, but reduces to pressure coordinate at higher levels near the tropopause.

(a) CAM4 Physics

All the three dynamical cores use the same physical parameterization package, consisting of moist precipitation processes, clouds and radiation processes, surface processes, and turbulent mixing processes. Each of these in turn is subdivided into various components. The moist precipitation processes consist of the deep convective, shallow convective and stratiform components. The deep convective processes are parameterized by the revised version of the Zhang-McFarlane convection scheme, in which the calculation of CAPE has been modified to include the effect of entrainment dilution (Neale et al., 2008). In addition, in the revised version, convective momentum transport parameterized by Gregory et al. (1997) has been included (Richter and Rasch, 2008). The shallow convective process is parameterized by Hack (1994). The parameterization of the stratiform processes in CAM4 is described in Rasch and Kristjansson, (1998) and Zhang et al. (2003). In the

default configuration of the model, the parameterizations are applied over a time interval of 1200 s for EUL, 1800 s for FV, and 1800 s for HOMME.

(b) CAM4 Dynamical cores

The EUL dynamical core is a three-time-level, spectral transform applied at T85 truncation on a 256X128 quadratic grid. Moisture transport in EUL is done using a monotonic semi-Lagrangian method, which is time split in the horizontal and vertical directions. The trajectory calculation used for moisture transport uses a quasi-cubic interpolation. A detailed scientific documentation of the EUL dynamical core is given in the CAM3 scientific documentation (Neale et al. 2010).

CAM FV integrates the quasi-hydrostatic equations of motion in flux-form. The horizontal spatial discretization grid is based on a 'CD'-grid approach that involves a half-time-step update on the Arakawa C grid that provides the time-centered winds to complete a full time step on the Arakawa D grid (Lin and Rood 1997). In the vertical, a floating Lagrangian coordinate is used, that is initialized from a standard hybrid-sigma vertical coordinate (Eulerian grid). The Lagrangian vertical coordinate 'floats' for several consecutive time-steps (default setup for this study is 4) before a vertical remapping transfers the prognostic variables back to the Eulerian reference grid. The vertical remapping procedure is formulated so that it conserves total energy (Lin 2004). The advantage of the floating Lagrangian coordinate approach is that the equations of motion in each layer reduce to two-dimensional shallow water equations, hence, only two-dimensional operators are needed. The two-dimensional advection operator used in CAM-FV follows the Lin and Rood (1996) scheme. The water variables (specific humidity, cloud liquid water and ice) and tracers are transported on longer time-steps than that used for the

momentum, thermodynamic and continuity equation for air (setup in this study is 4 dynamics time-steps per tracer time-step) using super-cycling (e.g., Lin 2004). The Lin and Rood (1996) advection scheme applies a combination of Piecewise Constant and Piecewise Parabolic Methods (Colella and Woodward 1984) in its dimensionally split one-dimensional operators. The stability properties of this configuration (and others) are discussed in detail in Lauritzen (2007). The moisture transport in CAM-FV is computed with the Lin and Rood (1996) transport scheme, which is a flux-form finite-volume scheme, formulated in terms of one-dimensional operators. The flux-operators are based on the Piecewise Parabolic Method (PPM, Colella and Woodward, 1984) that are formally third-order accurate on uniform grids, and hence the implementation on the regular latitude-longitude grid is formally second order. The damping and dispersion properties of the scheme are discussed in Lauritzen (2007). Monotonicity is enforced using reconstruction function filtering in each coordinate direction which prevents negative undershoots in each coordinate direction. The discretization in CAM FV is such that vorticity modes at the grid scale are controlled through sub-grid-scale function limiters in the advection operator. Divergent modes, however, are not controlled at the grid scale through limiters wherefore explicit second-order divergence damping is applied to the momentum equations. To stabilize the model in the presence of gravity waves, one-dimensional polar filters are applied along latitudes. More information on CAM-FV and the performance in idealized tests can be found in Lauritzen et al. (2010). Diffusion in CAM-FV is through the monotonicity constraints in the advection operator as well as explicitly added divergence damping (Neale et. al. 2010).

HOMME uses the continuous Galerkin spectral finite element method (Taylor et al., 2010), often abbreviated as the spectral element method (SEM). This method is designed

for fully unstructured quadrilateral meshes. The current configurations in CAM are based on the cubed-sphere grid. The main motivation for the inclusion of HOMME is to improve the scalability of CAM by introducing quasi-uniform grids, which require no polar filters (Taylor et al., 2008). HOMME is also the first dynamical core in the CAM that locally conserves energy in addition to mass and two-dimensional potential vorticity (Taylor, 2010). HOMME represents a large change in the horizontal grid as compared to the other dynamical cores in CAM. Almost all other aspects of HOMME are based on a combination of well-tested approaches from the Eulerian and FV dynamical cores. For tracer advection, HOMME is modeled as closely as possible on the FV dynamical core. It uses the same conservation form of the transport equation and the same vertically Lagrangian discretization (Lin 2004). The HOMME dynamics are modeled as closely as possible on Eulerian dynamical core. They share the same vertical coordinate, vertical discretization, hyper-viscosity based horizontal diffusion, top-of-model dissipation, and solve the same moist hydrostatic equations. The main differences are that HOMME advects the surface pressure instead of its logarithm (in order to conserve mass and energy), and HOMME uses the vector-invariant form of the momentum equation instead of the vorticity-divergence formulation. The time stepping in HOMME is a form of dynamics/tracer/physics sub-cycling, achieved through the use of multi-stage 2nd order accurate Runge-Kutta methods. The tracers and dynamics use the same time step, which is controlled by the maximum anticipated wind speed, but the dynamics uses more stages than the tracers in order to maintain stability in the presence of gravity waves.

The moisture transport in CAM-HOMME is computed with the same vertically Lagrangian approach (Lin 2004) as used in CAM-FV, and the former uses the monotone vertical remap from (Zerroukat et al, 2005). The transport within the Lagrangian surfaces is

done using the locally mass conserving spectral element discretization (Taylor and Fournier, 2010), combined with a sign-preserving limiter (Taylor et al., 2009). The spectral element advection operator is 4th order accurate on the cubed-sphere grid with very little diffusion, so additional scale selective mixing is added via the same hyper-viscosity term used in the dynamics (Neale et al., 2010). The spatial diffusion used in CAM-HOMME is modeled on that used in CAM-Eulerian. CAM-HOMME uses the same hyper-viscosity operator, and the 1-degree results presented here use the same hyper-viscosity coefficient as T85 CAM-Eulerian. The hyper-viscosity operator is solved explicitly and time-split from the rest of the dynamics, using a mixed finite element integrated-by-parts formulation (Neale et al., 2010).

3 Simulation Details

For the examination of the performance of HOMME in NCAR-CAM4, we carried out a set of simulations with HOMME, FV (the default dynamical core of CAM4), and EUL. All the simulations were performed in the aqua-planet configuration of CAM4. In this configuration, all the land points are replaced by ocean points such that the surface drag coefficients, albedo, and evaporation characteristics are homogeneous over the globe. A further simplification is obtained by fixing the solar declination to its value on March 21, which puts the sun overhead at the equator. This produces another desirable simplification by providing approximate hemispheric symmetry of insolation forcing. The experiments have been performed with a zonally symmetric SST profile as lower boundary condition. The distribution of SST used in the simulation is given in equation 1, which is the same as the control SST used by Neale and Hoskins (2000):

$$T_s(\lambda, \phi) = \begin{cases} 27[1 - \sin^2(3\phi/2)]^0 \text{C} & : -\pi/3 < \phi < \pi/3 \\ 0^0 \text{ C} & : \text{Otherwise} \end{cases} \quad (1)$$

where, T_s =Sea Surface Temperature (^0C), λ = longitude, ϕ = latitude.

The initial condition for all simulations was from a previous aqua-planet simulation. All the simulations were performed for 24 months, and the last 18 months were considered for the analysis. The default physics tunings were used for all the simulations. The monthly and daily model outputs have been analyzed to understand various issues pertaining to the steady (time mean) and transient (temporally varying) characteristics of simulated climate.

4 Results

(a) Instantaneous Distribution

Figure 1 shows the horizontal distribution of the total precipitation at the surface from FV, EUL, and HOMME. The left column of the figure shows the instantaneous features, and the right column shows the time mean features. For the study of the instantaneous features, several snapshots were analyzed and the basic characteristics were found to be similar. One representative instant has been arbitrarily chosen for illustration. The storm-like zonally oriented structures in the tropics and baroclinic wave-like meridionally oriented structures in the mid-latitudes are evident in all the three dynamical cores (see the left column). The interactions between the tropics and extra-tropics show up prominently in the instantaneous

patterns. The time mean features shown in the right column are the average of the instantaneous features. The inter-tropical convergence zone (ITCZ) appears over the equator saliently. The dry zones over sub-tropical highs are distinct. The secondary rainfall zones over mid-latitude storm tracks are also distinctly clear in all the three dynamical cores. The notable difference is that the ITCZ in EUL and HOMME is comparatively sharper and more confined to the equator than that in FV. By and large, the horizontal distribution of rainfall is found to be similar in all the three dynamical cores.

Since the HOMME dynamical core is based on the cubed-sphere grid, it is desirable to examine the wave-4 signal from the simulations. In figure 2, the difference in the time averaged precipitation and its zonal mean is shown. However, no signature of the wave-4 is evident in the plot. This indicates that the simulation is devoid of such noise and the length of integration is long enough. The other two dynamical cores are based on lat-lon grid and known to be free from wave-4 noise.

(b) Mean State

In this section we compare the time mean state of precipitation from FV, EUL, and HOMME. Figure 3 shows the zonally averaged time-mean surface reaching total rainfall (TRF) for the three dynamical cores. We find that the peak of the ITCZ is over the equator in all the three cases. The morphology of the ITCZ is found to be similar. However, there is notable difference in the magnitude of the TRF. Over the equator, the TRF in EUL and HOMME is higher than that in FV. The mean TRF over the equator in FV is ~ 18 mm/day, whereas in EUL & HOMME it is around 25 mm/day. The difference is around 40% of the mean value of FV. However, there is almost no difference in TRF between EUL & HOMME. Since TRF constitutes of three components, namely, deep convective rainfall

(DRF), shallow convective rainfall (SRF), and large-scale rainfall (LRF), in the following we analyze them individually.

Figure 4 shows the zonally averaged time mean surface reaching DRF, SRF, and LRF, for FV, EUL, and HOMME. All the three components are found to be higher in EUL than that in FV. Among the three components, the difference in DRF between EUL and FV dominates the other two components. On the contrary, the comparison between FV and HOMME indicates that DRF is almost same for both of them, whereas the other two components are higher in HOMME than that in FV. The difference in LRF between HOMME and FV is nearly double of the difference in SRF. In other words, the higher TRF in EUL is primarily due to more DRF, whereas in HOMME it is mainly due to more LRF.

Since rainfall simulation is sensitive to time step (Williamson and Olson, 2003; Mishra et al., 2008) and is different in the three dynamical cores, we will examine its contribution to the differences in the three simulations. In order to do so, we carried out two additional simulations with FV and HOMME with 1200 s. Figure 5 shows the zonally averaged time mean precipitation from the three simulations. It is noticed that TRF is largely similar in EUL and HOMME, and more than that in FV. Higher TRF in EUL is primarily due to more DRF, whereas in HOMME it is mainly due to more LRF. The result is similar to that seen in the simulations with default time steps. This infers that, the difference in the simulations with the three dynamical cores is not due to different physics time steps, rather due to the difference associated with the formulation of the dynamical cores and their indirect effects through the physics parameterization. However, TRF is found to be marginally increasing with the reduction of time step, which is due to the enhancement in LRF. This result is in agreement with Mishra et al. (2008). They showed that TRF and LRF increase with decrease in time step and the impact is less severe in the

smaller time step regime.

The surface reaching rainfall is the vertical integral of the net precipitation production at each model level. The net precipitation production at any level is the condensation minus re-evaporation of precipitation and cloud liquid water at that corresponding level. In figure 6, the vertical distribution of the net precipitation production is shown for FV, EUL, and HOMME. The first column shows the vertical distribution of the TRF production. Similarly, the second, third, and fourth columns show the vertical distribution of DRF, SRF, and LRF respectively. The figure shows that in all three cases the net TRF production is vertically extended over the entire troposphere, except for a few near-surface and top of the model layers. The latitudinal extent and vertical distribution of TRF looks alike in the three dynamical cores. The altitude of peak TRF occurs around the same level. However, there is a notable difference in their magnitudes i.e., TRF in EUL and HOMME is more than that in FV, which is in agreement with the preceding discussion. In all the three cases, DRF occurs in the lower and mid troposphere, accompanied by re-evaporation of precipitation and cloud liquid water in the upper troposphere. The third column shows that there is very little SRF in FV, as compared to that found in EUL and HOMME. In all the three dynamical cores the SRF production occurs in the mid and lower troposphere with peaks at around 600 hPa. From the fourth column it can be seen that LRF occurs in the middle and upper troposphere. The peak of the LRF occurs at around 500 hPa in all the three cases. There is considerable amount of re-evaporation of LRF seen in the lower troposphere and near-surface layers. Overall, the vertical distribution of precipitation production is similar in the three dynamical cores.

In figure 6, it is seen that most of the precipitation occurs within the latitudinal belt of 5S to 5N. In order to make a closer comparison between the vertical profiles of

precipitation, we have shown the area averaged (0E-360E, 5S-5N) time-mean precipitation production rate for FV, EUL, and HOMME in figure 7. The figure shows a close resemblance in their profiles. The peak of the precipitation production occurs at around 600 hPa in all three cases. Near the surface (below 950 hPa), the net precipitation production is negative, which is due to the fact that the re-evaporation of falling precipitation is more in these layers. The notable point here is that there is a systematic difference in the magnitude of the precipitation production in the mid troposphere between the three cases. EUL has the largest precipitation production, whereas FV has the smallest, and HOMME falls in between these two.

In order to get an overall idea about the global mean values, we analyzed these quantities for the three dynamical cores. Table 1 shows the global mean TRF from FV, EUL, and HOMME. The values are very close to each other, i.e., difference among them is on the order of 2.5% of their mean values. Secondly, the global mean value for HOMME falls in between that of the other two dynamical cores.

(c) Intensity and Frequency

Here we show the intensity and frequency of rainfall for FV, EUL, and HOMME. For this we analyzed the daily rainfall data. Since in the preceding section we noticed that the region of significant difference is the deep tropics (0E-360E, 10S-10N), we will focus primarily on this region. Figure 8 shows the frequency distribution of daily rainfall rates (left panel) and the total rainfall falling in each bin (right panel). The rainfall rates are categorized into four categories, based on the intensity of rain rate, namely, dry, light, moderate, and heavy categories. Vertical lines in figure 8 indicate these categories. Figure 8a shows that the frequencies in the dry and heavy categories are higher in EUL and

HOMME than in FV. In the light and moderate categories the reverse is true. Although the frequencies in the dry category are higher, when the frequencies were multiplied with the respective rainfall rates (accumulated rainfall), they become almost equal in the three dynamical cores (see figure 8b). Secondly, the accumulated rainfall in the light and moderate categories are highest in FV, than in HOMME, and least in EUL. Whereas the rainfall accumulated in the heavy category is found to be higher in EUL and HOMME than that in FV. Hence, the higher amount of TRF in HOMME and EUL comes from the heavy rainfall category. There appears a mismatch between figures 8a and 8b, which is counter-intuitive, but this is because of the fact that within the categorized bin, there is an internal shift. For example, in heavy category, the frequency in EUL is higher than that in FV, whereas the accumulated rainfall in heavy category shows the reverse. We investigated by making finer bin size in this category and noticed that there was an internal shift towards the upper end in HOMME, i.e., there are more number of points with higher rainfall rates than that in EUL in the deep tropics.

(d) Time-Longitude Realization

The time mean features for FV, EUL, and HOME have been discussed in the previous section. Since the transients play a cumulative role in forming the time mean steady state, here we discuss the transient activities. In section 5-b we saw that the difference between the dynamical cores was mainly found in the equatorial belt, where most of the transient activities constitute the zonally propagating waves. Hence, we will consider this region and discuss the zonal propagation characteristics via time-longitude diagrams.

Figure 9 shows the time-longitude diagrams of rainfall over the equator (2.S to

2.5N) for 180 days. Daily data has been plotted in the figure. All of them (FV, EUL, and HOMME) show the eastward propagation. This resembles observed equatorial Kelvin waves (Wheeler and Kiladis 1999). These rainfall bands appear to move over a range of speeds and wave numbers, however there are distinct differences between the three cases.

In FV, eastward propagating organized rainfall bands appear. They propagate 360° in 30 to 40 days. While in EUL, the rainfall appears in patches in a discrete manner. The rainfall bands are not well organized. In HOMME, streaks of well-organized rainfall are noticed. They propagate 360° in 20 to 30 days. Since vertical structure of the moist heating is crucial in determining the speed of the eastward propagations, we have shown the same for the three dynamical cores in figure 10. The figure shows that the profiles are largely similar. All of them have most of their heating in the upper troposphere and have top-heavy heating structure. Comparison of FV and EUL indicates that throughout the troposphere, EUL has more heating rate than FV. The heating profile of HOMME largely falls in between the other two dynamical cores in the lower troposphere. However around 500 hPa, the heating in HOMME is closer to EUL and significantly more than that in FV. Hence, the top-heaviness in the heating profile is more in HOMME than FV. This is associated with the faster phase speed of the eastward propagation in HOMME.

(e) Associated Variables

In figure 11, the meridional variation of surface evaporation (EVP), large-scale moisture convergence (LMC) and vertically integrated precipitable water (PWAT) is shown for FV, EUL, and HOMME. Figure 11-a shows that EVP is highest for EUL, lowest for FV and intermediate for HOMME. Over the equatorial belt, LMC in EUL and HOMME are nearly same and more than that in FV (see figure 11-b). Local

evaporation and large-scale moisture convergence are the two sources of moisture for rainfall production. Comparison of the scales of the figure 11-a and 11-b indicates that LMC is the primary source of moisture leading to higher rainfall over the ITCZ in EUL and HOMME than in FV. PWAT is found to be almost same in all the three dynamical cores, except over the equator, where EUL has marginally more than that in FV and HOMME.

In CAM4, the surface evaporation is computed as shown below (Neale et al., 2010):

$$EVP = \rho_A |\Delta V| C_E dQ \quad (2)$$

where, ρ_A is the atmospheric surface density, and ΔV and dQ are the wind strength and moisture deficit at the lowest model level, respectively. Figure 12-a shows that moisture (Q) at the 1st model level is almost same in EUL and HOMME and lower than that in FV. In other words, dQ in EUL and HOMME is higher than that in FV. Figure 12-b shows that wind strength at the lowest level of the model is higher in EUL than in HOMME and FV over the equatorial belt. However beyond 5S/N the wind strength in EUL and HOMME is lesser than that in FV. Hence, the higher evaporation in EUL over the equatorial belt is attributed partly to higher dQ and partly to the higher wind speed than that in FV. Beyond 5S/N the higher evaporation is solely due to the higher moisture deficit, since the wind speed therein is lesser than FV. However, the higher EVP in HOMME over the equatorial belt is primarily due to the higher moisture deficit, since the wind speed therein is almost same as FV.

Figure 13 shows the convective available potential energy (CAPE) for FV, EUL, and HOMME. It is seen that over the equatorial belt, EUL has significantly higher CAPE than FV and HOMME, which is around 135% of the mean CAPE in FV. This is the reason

for the higher amount of deep convective rainfall in EUL. However, there is no such significant difference in CAPE between FV and HOMME, leading to similar magnitudes of DRF.

The vertical profiles of area averaged (0E-360E, 5S-5N) time mean relative humidity (RH), specific humidity (Q), and temperature (T) are compared in figure 14. RH is found to be lesser (by around 3%) in HOMME than FV, over the whole troposphere except at 900 hPa. On the contrary, RH in EUL is found to be higher (by around 4%) in most of the layers, except those adjacent to the surface and between 900-700 hPa, where the reverse is true. Figures 14-b and 14-c show the corresponding specific humidity and temperature differences. It is seen that, in the middle and lower troposphere, the profile of the difference in specific humidity resembles very closely to that of the difference in RH, which is further supported by the observed temperature profiles (see figure 14-c). In the upper troposphere, the lesser RH in HOMME and higher RH in EUL are mainly because of the higher temperature in HOMME and lower temperature in EUL, respectively, since the difference in Q in these altitudes is almost negligible. Moisture in the boundary layer but above the surface layer (around 900 hPa) is greater in EUL than that in FV and HOMME, which seems to be associated with the higher CAPE in EUL.

(f) General Circulation Diagnostics

Generally the largest spatial variation of atmospheric quantities occurs in the vertical and meridional directions, so analysis of the lat-height cross-section of zonal mean quantities is a useful exercise and provides an insight into the general circulation of the atmosphere. For this we analyzed temperatures, zonal wind, vertical velocity, and specific humidity from the three dynamical cores.

In figure 15, zonal mean temperatures are shown from FV, EUL, and HOMME. In general, the similarity between the three distributions is remarkable. The pole-to-equator temperature difference is about 30° C at the earth's surface. The latitudinal temperature gradient is identical in all of them. In the lower stratosphere the temperatures increase by about 25° C from the equator to mid-latitudes, but decrease again with a further increase in latitudes. The magnitude and altitude of the tropopause temperatures is similar in all of them. The pole-to-equator difference of the height of the tropopause in the model is similar in all the three dynamical cores. In high latitudes a stable layer appears primarily due to the stabilizing effects of baroclinic waves and poleward advection of heat by the large scale eddies. In the upper stratosphere, the decrease of temperatures from equator to pole is about 25° C. We further examined the vertical profile of temperatures at various latitudes from the three dynamical cores. The notable difference noticed (not shown here) is, over the equatorial region the atmosphere is marginally ($\sim 0.5^{\circ}$ C) warmer in HOMME than that in FV. Between EUL and FV, EUL has a warmer (by $\sim 0.5^{\circ}$ C) atmosphere in the lower troposphere and stratosphere, however, a cooler atmosphere in the middle and upper troposphere. In general, the thermal structure of the model atmosphere looks very similar in the three dynamical cores.

Figure 16 shows the longitudinal mean zonal wind for FV, EUL, and HOMME. The patterns of the lower tropospheric easterlies and the upper tropospheric westerlies look similar. Intensity of the jet and its spatial position agree well. It is found that, the regions of largest latitudinal gradient in temperature (Fig. 15) are coincident with those of the highest vertical gradient of zonal wind in Fig. 16. This confirms that, the two fields are close to a state of thermal wind balance. Similarly mean meridional circulation was analyzed from the three dynamical cores (not shown here). It was noticed that the positions of the ITCZ and

positions of the strongest ascent are at the same latitudes, which was anticipated. The notable differences between the three cases are the following: in EUL the circulation over the equatorial belt is marginally stronger. The rising limb of the Hadley cell shifts towards the equator in EUL, associated with strong surface winds over the equatorial belts. This strengthening of the circulation, in turn, leads to an increase in the moisture convergence into the equatorial region. However, the zonal and meridional circulation is found to be largely similar in all of them.

Zonally averaged time-mean vertical pressure velocity (ω) is shown in figure 17, for FV, EUL, and HOMME. A negative value of ω is associated with ascending motion, which is indicated by the dashed contours. It is observed that, the ascending limb is more confined to the equator in EUL and HOMME. The latitudinal positions of the maximum ω are noticed over the corresponding locations of ITCZ, i.e., over the equator. The altitude of maximum ω occurs in the lower troposphere in all of them. Notable is the difference in strengths of ω . The strength is largely similar in EUL and HOMME, but greater than that in FV. Previously, in figure 10 it was seen that, the rate of moist heating over the equatorial region is higher in EUL and HOMME, which is associated with the stronger vertical velocity.

Finally, the distribution of specific humidity from the three dynamical cores is shown in figure 18. The very dry upper troposphere and stratosphere, the wet lower troposphere, and the dry subtropics are common in all of them. The spatial pattern of specific humidity and its magnitude are similar. It has a maximum over the surface layer of the equatorial belt and decreases with increase in altitude and/or latitude. This is associated with the fact that the primary source of moisture, i.e., surface evaporation occurs in the lowest model level, which is strongest in the tropics and decreases with increase in

latitudes. Furthermore, the moisture sink, i.e., precipitation removes the moisture from the mid and upper troposphere. Large-scale circulation redistributes the moisture in the atmosphere, makes it moister in convergence zone (e.g. ITCZ) and makes it drier in the divergence zone (e.g. subtropical highs). The combined effect of the three factors governs such a distribution of the moisture in the atmosphere. The vertical and meridional gradient of the specific humidity is similar in all of them. By and large, the distribution of specific humidity is similar. However, comparison of the vertical profiles from the three dynamical cores over individual latitudes showed marginal differences (not shown here). For instance, over the equatorial belt, the surface layer is comparatively more moist in FV, but in the lower troposphere (around 900 hPa) the reverse is true. However, in the upper troposphere, EUL is found to have the highest specific humidity, followed by FV, and HOMME, respectively.

5 Summary and Conclusions

The High Order Method Modeling Environment (HOMME) is a new spectral element-based dynamical core included in the CCSM4. HOMME is a highly scalable dynamical core that achieves the conservation of mass, potential vorticity (in 2D), and moist energy. HOMME has been integrated into the Community Atmospheric Model version 4 (CAM4), the atmospheric component of the CCSM. Initial simulations have been completed in the aqua-planet configuration of CAM4. The results have been examined to assess their fidelity in the simulation of rainfall, one of the most important components of the Earth's climate system. For this, comparison has been made with the results from the other two existing dynamical cores of CAM4, namely, finite volume (FV) and Eulerian (EUL).

The instantaneous distribution of rainfall has been compared from the three dynamical cores. The storm-like zonally oriented structure in the tropics and baroclinic wave-like meridionally oriented structures in the mid-latitudes are observed in all of them. The interactions between the tropics and extra-tropics show up prominently. The characteristics of the horizontal distribution of rainfall in HOMME are found to be similar to that in FV and EUL.

The zonally averaged time-mean rainfall has been compared for HOMME, FV, and EUL. The inter tropical convergence zone (ITCZ) has a single peak morphology in all the three simulations. However, there is a considerable difference in the strength of the ITCZ. The amount of rainfall in ITCZ is found to be almost same in HOMME and EUL, which is around 135% of that in FV. It is shown that the moisture deficit at the 1st model level (as compared to the saturation value at surface temperature) in HOMME is more than that in FV, which leads to higher surface evaporation. This higher surface evaporation leads to higher large-scale moisture convergence into the ITCZ, which leads to higher rainfall. The mechanism of higher rainfall in EUL is similar to the preceding, only with the following extra link. In EUL, the wind strength at the 1st model level is higher than that in FV, which is an additional factor responsible for the higher surface evaporation in EUL.

The vertical distribution of the precipitation production has been compared from HOMME, FV, and EUL. The vertical profile is found to be similar. The maximum precipitation production takes place at around 600 hPa. The net precipitation production is negative below 950 hPa, which is because of the re-evaporation of precipitation. Largely, the vertical structure of the precipitation is similar in all the three dynamical cores.

The daily rainfall data has been examined from HOMME, FV, and EUL to study the intensity and frequency characteristics of rainfall. On the basis of intensity, rainfall is

categorized as dry, light, moderate or heavy. The notable difference is that, the frequency of rainfall in the dry and heavy intensity categories is higher in HOMME and EUL than FV. On the contrary, in the light and moderate categories, the frequency of rainfall in EUL and HOMME is lesser than that in FV. However, EUL and HOMME show very similar characteristics. The propagation characteristics of the rainfall band have been examined from the three dynamical cores. Well-organized coherent eastward propagation is noticed in both HOMME and FV, however, the coherence is much less in EUL.

We thus conclude that, the rainfall simulated by HOMME falls in a regime somewhere in between that of FV and EUL. Future work includes the investigation of the performance of HOMME in a real-planet framework having realistic earth geography.

Acknowledgements

Many researchers have participated in the development of HOMME. We thank Amik St-Cyr, John Dennis, Jim Edwards, Rich Loft, Rory Kelly and Theron Voran for their contributions to HOMME development. We are grateful to Phil Rasch and Dave Williamson for many fruitful discussions. The research is supported by DOE, grant no. DE-F402-07ER64464.

References

Colella, P., and P. R. Woodward, 1984: The Piecewise Parabolic Method (PPM) for gas-dynamical simulations. *J. Comput. Phys.*, 54, 174-201.

Dennis, J., A. Fournier, W. F. Spitz, A. St.-Cyr, M. Taylor, S. J. Thomas, H. Tufo, 2005: High Resolution Mesh Convergence Properties and Parallel Efficiency of a Spectral Element Atmospheric Dynamical Core, *Int. J. High Perf. Computing Appl.*, 19 225–235.

Edwards J, and coauthors, 2011: CAM-HOMME: A scalable spectral element dynamical core for the Community Atmosphere Model, *Int. J. High Perf. Computing Appl.*, under review.

Gregory, D., R. Kershaw, and P. M. Inness, 1997: Parameterization of momentum transport by convection. II: Tests in single-column and general circulation models, *Q. J. R. Meteorol. Soc.*, 123, 1153–1183.

Hack, J. J., 1994: Parameterization of moist convection in the National Center for Atmospheric Research Community Climate Model (CCM2), *J. Geophys. Res.*, 99, 5551-5568.

Lauritzen, P. H., 2007: A Stability Analysis of Finite-Volume Advection Schemes Permitting Long Time Steps. *Mon. Wea. Rev.* 135, 2658-2673.

Lauritzen, P.H., C. Jablonowski, M.A.Taylor, and R.D. Nair, 2010: Rotated versions of the Jablonowski steady-state and baroclinic wave test cases: A dynamical core intercomparison. *Journal of Advances in Modeling Earth Systems.*, in press.

Lin, S.-J., and R. B. Rood, 1996: Multidimensional flux-form semi-Lagrangian transport schemes. *Mon. Wea. Rev.*, 124, 2046-2070.

Lin, S.-J., and R. B. Rood, 1997: An explicit flux-form semi-lagrangian shallow-water model on the sphere. *Quart. J. Roy. Meteor. Soc.*, 123, 2477-2498.

Lin, S.-J., 2004: A “vertically Lagrangian” finite-volume dynamical core for global models. *Mon. Wea. Rev.*, 132, 2293-2307.

Mishra. S. K., J. Srinivasan, and R. S. Nanjundiah, 2008: The impact of time step on the intensity of ITCZ in aqua-planet GCM. *Mon. Wea. Rev.*, 136, 4077 – 4091.

Nair, R. D., H. M. Tufo, 2007: Petascale atmospheric general circulation models. SciDAC 2007, June 24-28, Boston, USA. *J. Phys. Conf. Ser.*, 78, 1-5

Nair, R. D., H-W. Choi, and H. M. Tufo, 2009: Computational aspects of a scalable high-order discontinuous Galerkin atmospheric dynamical core. *Computers & Fluids*, Vol. 38, 309-319.

Neale, R. B. and B. J. Hoskins, 2000: A standard test for AGCMs including their physical parameterizations. I: The proposal. *Atmos. Sci. Lett.*, 1, 101-107.

Neale, R. B., J. H. Richter and M. Jochum, 2008: The impact of convection on ENSO: From a delayed oscillator to a series of events *J. Climate*, 21, 5904-5924.

Neale, R. B., and coauthors, 2010: Description of the NCAR Community Atmosphere Model (CAM4). Tech. Rep. NCAR/TN+STR, National Center for Atmospheric Research, Boulder, CO, 194 pp.(Available online at <http://www.cesm.ucar.edu/models/ccsm4.0/cam/>.)

Rasch, P.J. and J. E. Kristjansson, 1998: A comparison of the CCM3 model climate using diagnosed and predicted condensate parameterizations. *J. Climate*, 11, 1587-1613.

Richter, J. H., and P. J. Rasch, 2008: Effects of convective momentum transport on the atmospheric circulation in the community atmosphere model, version 3, *J. Climate*, 21, 1487–1499.

Taylor, M. A., J. Edwards, S. Thomas and R. Nair, 2007: A mass and energy conserving spectral element atmospheric dynamical core on the cubed-sphere grid, *J. Phys. Conf. Ser.* 78, doi: 10.1088/1742-6596/78/1/012074.

Taylor, M. A., J. Edwards and A. St-Cyr, 2008: Petascale atmosphere models for the community climate system model: a new development and evaluation of scalable dynamical cores, *J. Phys. Conf. Ser.*, 125, 1-10.

Taylor, M. A., A. St-Cyr, and A. Fournier, 2009: A non-oscillatory advection operator for the compatible spectral element method, *Computational Science ICCS Part II, Lecture Notes in Computer Science 5545 (Berlin / Heidelberg), Springer*, 273–282.

Taylor, M. A. 2010: Conservation of mass and energy for the moist atmospheric primitive equation on unstructured grids, in *Numerical Techniques for Global Atmospheric Models, Lecture Notes in Computational Science and Engineering*, Springer. (to appear)

Taylor, M. A. and A. Fournier, 2010: A compatible and conservative spectral element method on unstructured grids, *J. Comput. Phys.*, 229, 5879-5895.

Wheeler, M., and G. N. Kiadis, 1999: Convectively coupled equatorial waves: Analysis of clouds and temperature in the wavenumber-frequency domain. *J. Atmos. Sci.*, 56, 374-399.

Williamson, D.L. and J. G. Olson, 2003: Dependence of aqua-planet simulations on time step. *Quart. J. R. Meteorol. Soc.* 129, 2049-2064.

Zerroukat, M., N. Wood, and A. Staniforth, 2005: A monotonic and positive-definite filter for a semi-lagrangian inherently conserving and efficient (slice) scheme, *Q. J. R. Meteorol. Soc.*, 131 (611).

Zhang, M., W. Lin, C. S. Bretherton, J. J. Hack, and P. J. Rasch, 2003: A modified formulation of fractional stratiform condensation rate in the NCAR community

atmospheric model CAM2, *J. Geophys. Res.*, 108 (D1).

Figure Captions

Figure 1: Horizontal distribution of the total precipitation rate (mm/day) at the surface from FV, EUL, and HOMME. The left column shows the instantaneous distributions and the right column shows the time mean states. Notations used: FV for finite volume, EUL for Eulerian, and HOMME for high order method modeling environment.

Figure 2: Difference in the time averaged TRF (mm/day) and its zonal mean from HOMME.

Figure 3: Zonally averaged time mean total rainfall (TRF) from FV, EUL, and HOMME.

Figure 4: Zonally averaged time mean DRF, SRF, and LRF from FV, EUL, and HOMME. Notations used: DRF for deep convective rainfall, SRF for shallow convective rainfall, and LRF for large-scale rainfall.

Figure 5: Zonally averaged time mean TRF, DRF, SRF, and LRF from FV, EUL, and HOMME with 1200 s physics time step.

Figure 6: Vertical distribution of the net precipitation production for each component of the rainfall from FV, EUL, and HOMME. The shown quantities are the zonally averaged time mean values. Unit of all the quantities are in gram/kg/day.

Figure 7: Vertical profile of the area averaged (0E to 360E and 5S to 5N), time mean

precipitation production rate from FV, EUL, and HOMME.

Figure 8: (a) Frequency distribution of daily total rainfall (TRF) in the tropics (0E to 360E and 10S to 10N) for 90 days from FV, EUL, and HOMME. (b) Amount of TRF falling into each of the bins from FV, EUL, and HOMME.

Figure 9: Longitude-Time diagrams of daily rainfall (mm/day) averaged between 2.5S - 2.5N from (a) FV, (b) EUL, and (c) HOMME.

Figure 10: Vertical profile of the area averaged (0E to 360E and 2.5S to 2.5N) time mean moist heating from FV, EUL, and HOMME.

Figure 11: Zonally averaged time mean surface evaporation (mm/day), large-scale moisture convergence (mm/day), and precipitable water (kg/m²) from FV, EUL, and HOMME.

Figure 12: Zonally averaged time mean moisture deficit (gram/kg) and wind strength (m/s), at the 1st model level from FV, EUL, and HOMME.

Figure 13: Zonally averaged time mean convective available potential energy (CAPE) from FV, EUL, and HOMME.

Figure 14: (a) Vertical profile of the area averaged (0E to 360E and 5S to 5N) time mean relative humidity for (EUL-FV) and (HOMME-FV). (b) Same as figure-a but for specific humidity. (c) Same as figure-a but for temperature. Notations used: RH for relative

humidity, Q for specific humidity, and T for temperature.

Figure 15: Zonally averaged time mean temperature (K) for (a) FV, (b) EUL, and (c) HOMME.

Figure 16: Zonally averaged time mean zonal wind (m/s) for (a) FV, (b) EUL, and (c) HOMME.

Figure 17: Zonally averaged time mean pressure vertical velocity (Pa/s) for (a) FV, (b) EUL, and (c) HOMME

Figure 18: Zonally averaged time mean specific humidity (g/kg) for (a) FV, (b) EUL, and (c) HOMME.

Table Caption

Table 1. Global mean total rainfall (mm/day) from the three dynamical cores.

Figures

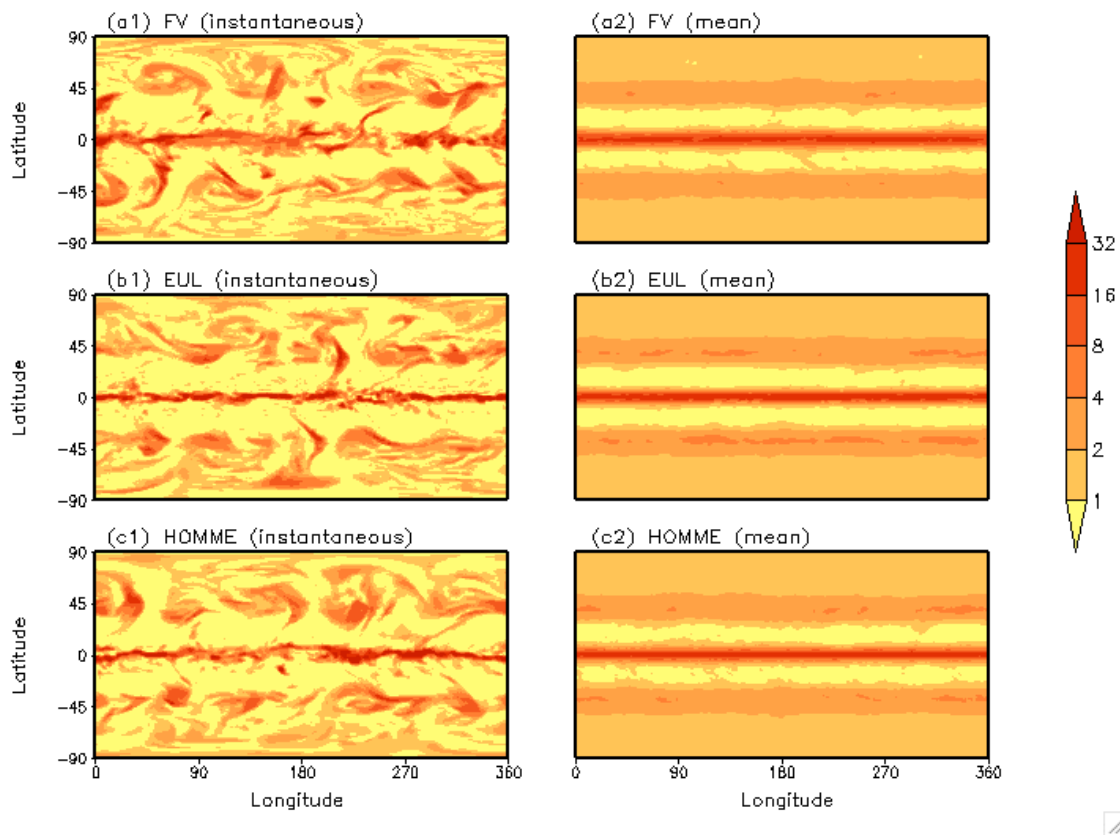


Figure 1: Horizontal distribution of the total precipitation rate (mm/day) at the surface from FV, EUL, and HOMME. The left column shows the instantaneous distributions and the right column shows the time mean states. Notations used: FV for finite volume, EUL for Eulerian, and HOMME for high order method modeling environment.

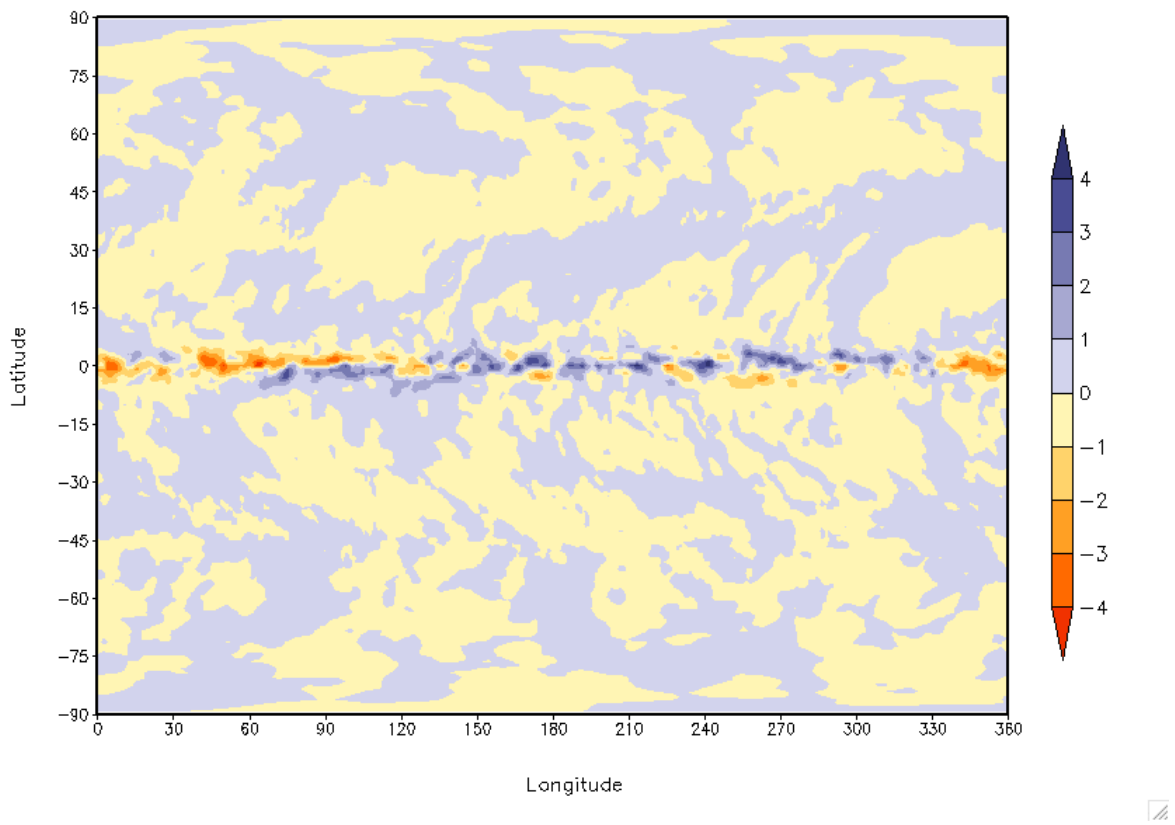


Figure 2: Difference in the time averaged TRF (mm/day) and its zonal mean from HOMME.

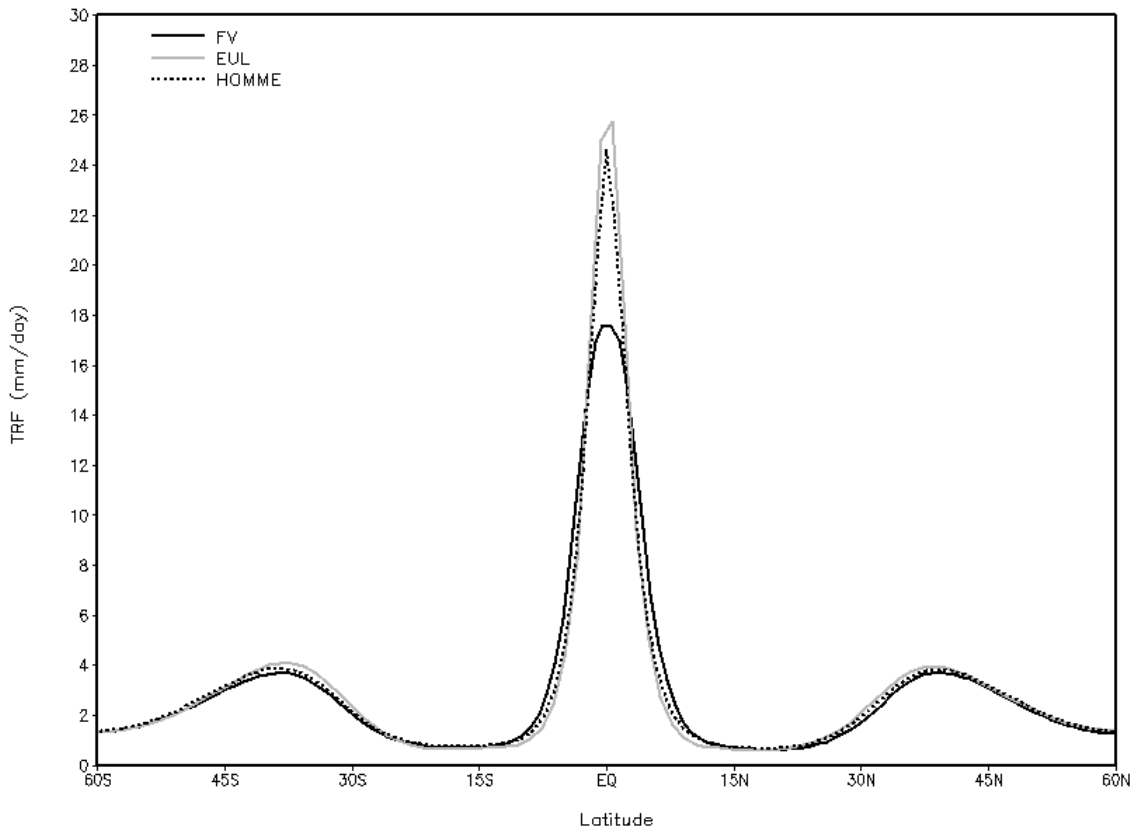


Figure 3: Zonally averaged time mean total rainfall (TRF) from FV, EUL, and HOMME.

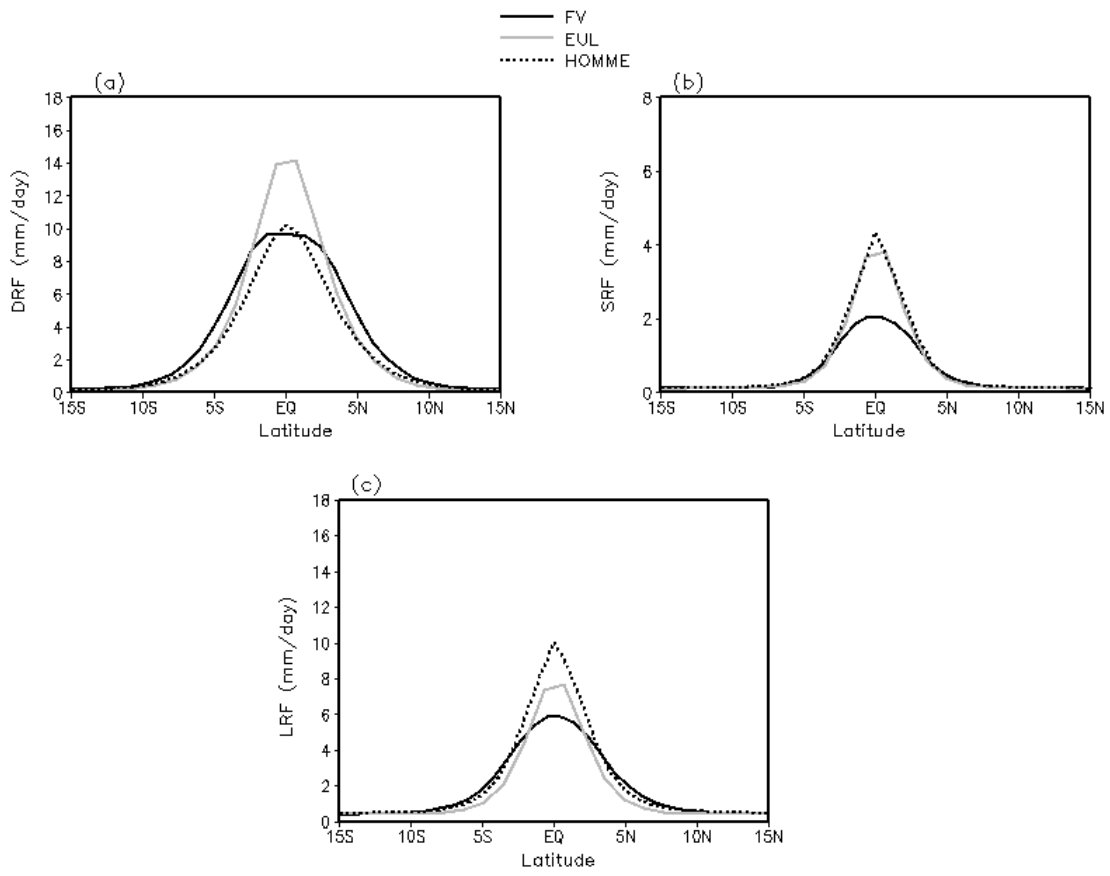


Figure 4: Zonally averaged time mean DRF, SRF, and LRF from FV, EUL, and HOMME. Notations used: DRF for deep convective rainfall, SRF for shallow convective rainfall, and LRF for large-scale rainfall.

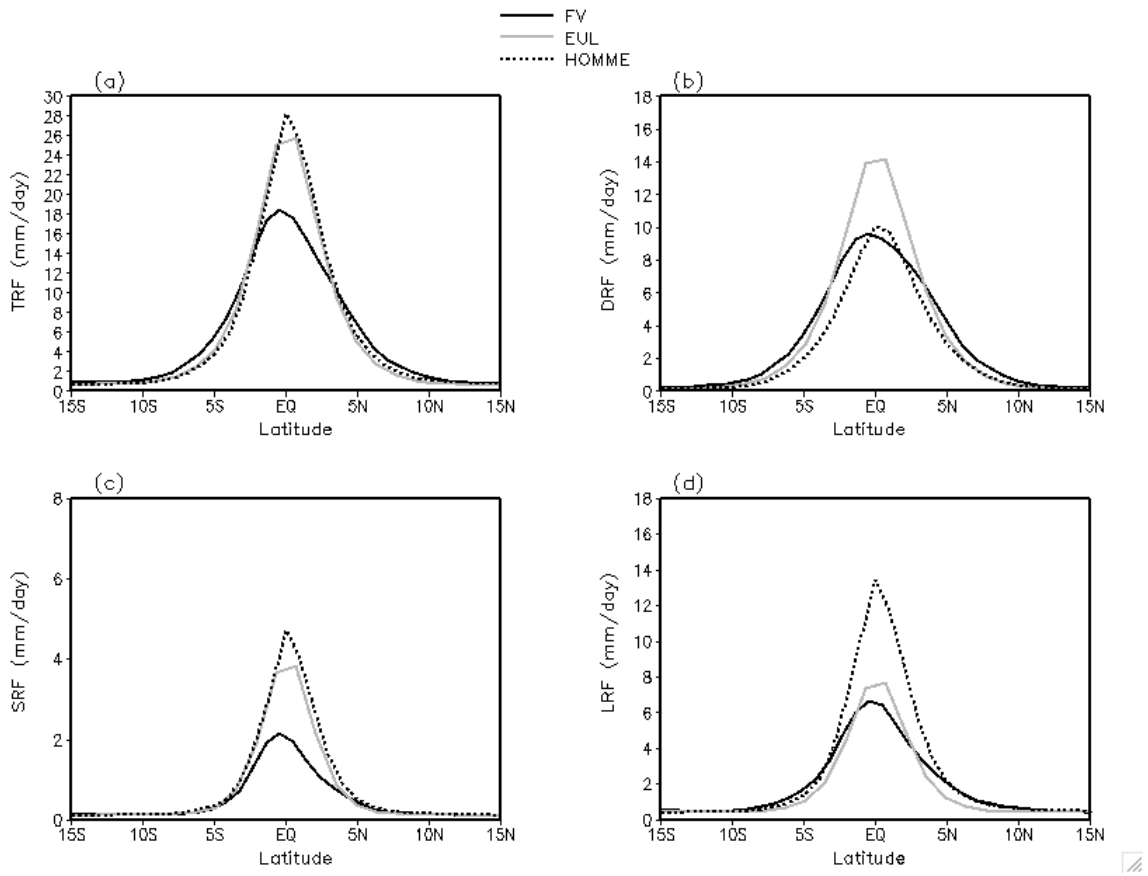


Figure 5: Zonally averaged time mean TRF, DRF, SRF, and LRF from FV, EUL, and HOMME with 1200 s physics time step.

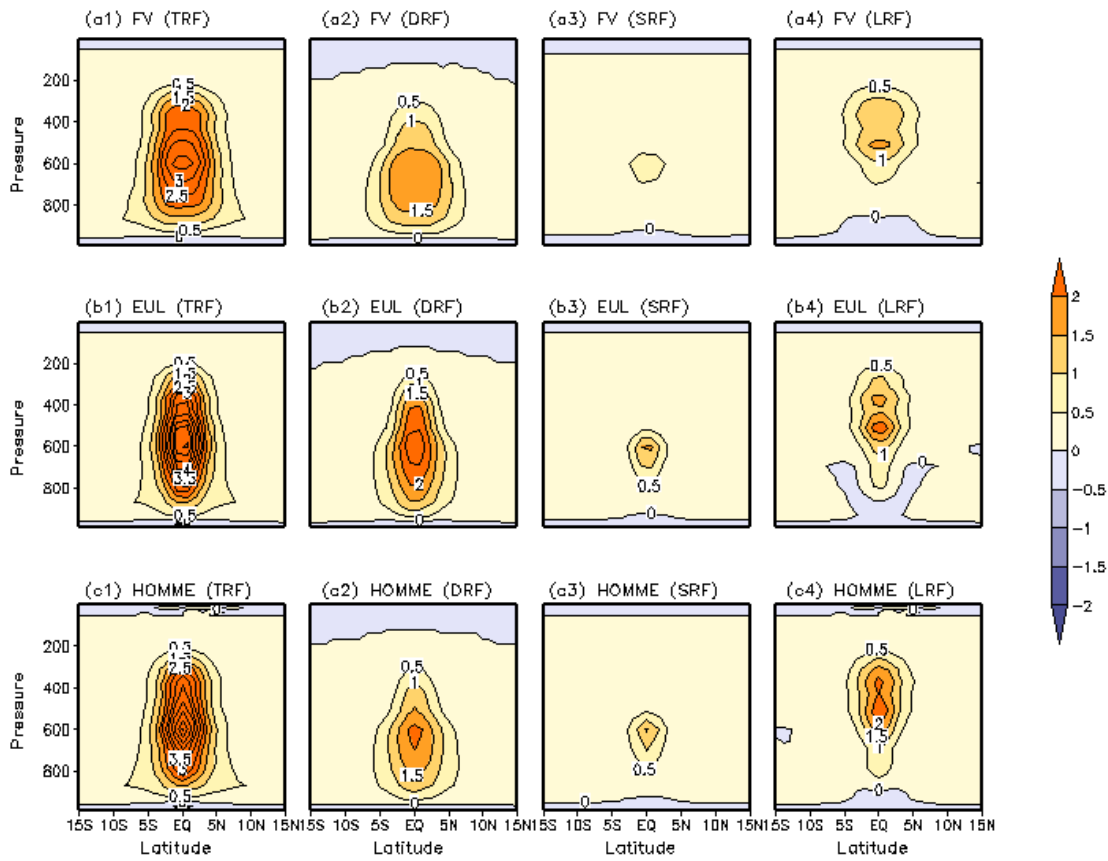


Figure 6: Vertical distribution of the net precipitation production for each component of the rainfall from FV, EUL, and HOMME. The shown quantities are the zonally averaged time mean values. Unit of all the quantities are in gram/kg/day.

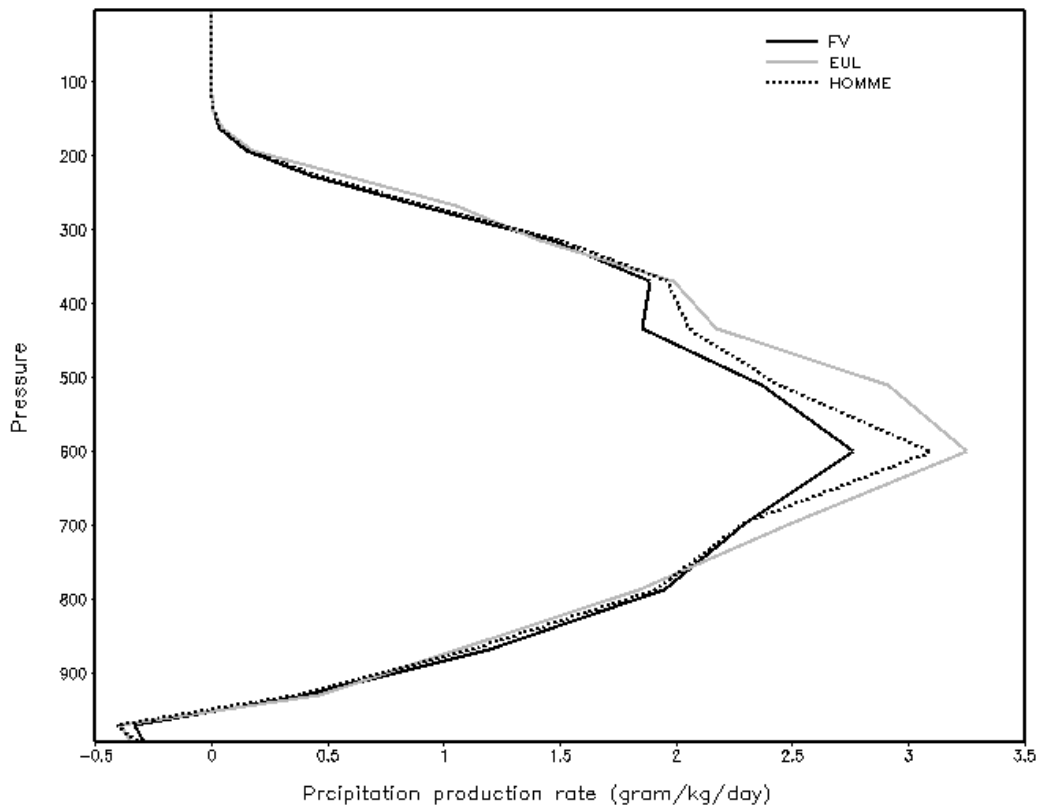


Figure 7: Vertical profile of the area averaged (0E to 360E and 5S to 5N), time mean precipitation production rate from FV, EUL, and HOMME.

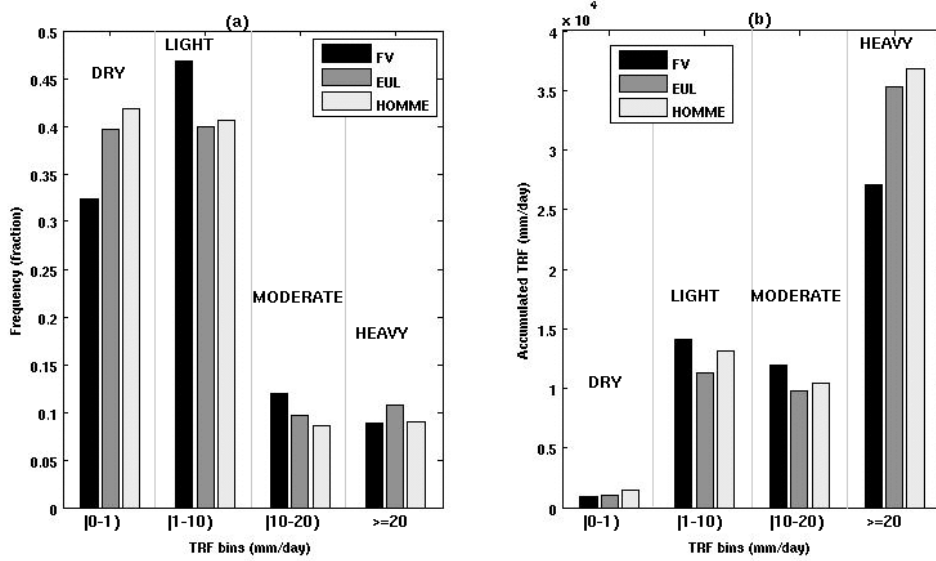


Figure 8: (a) Frequency distribution of daily total rainfall (TRF) in the deep tropics (0E to 360E and 10S to 10N) for 90 days from FV, EUL, and HOMME. (b) Amount of TRF falling into each of the bins from FV, EUL, and HOMME.

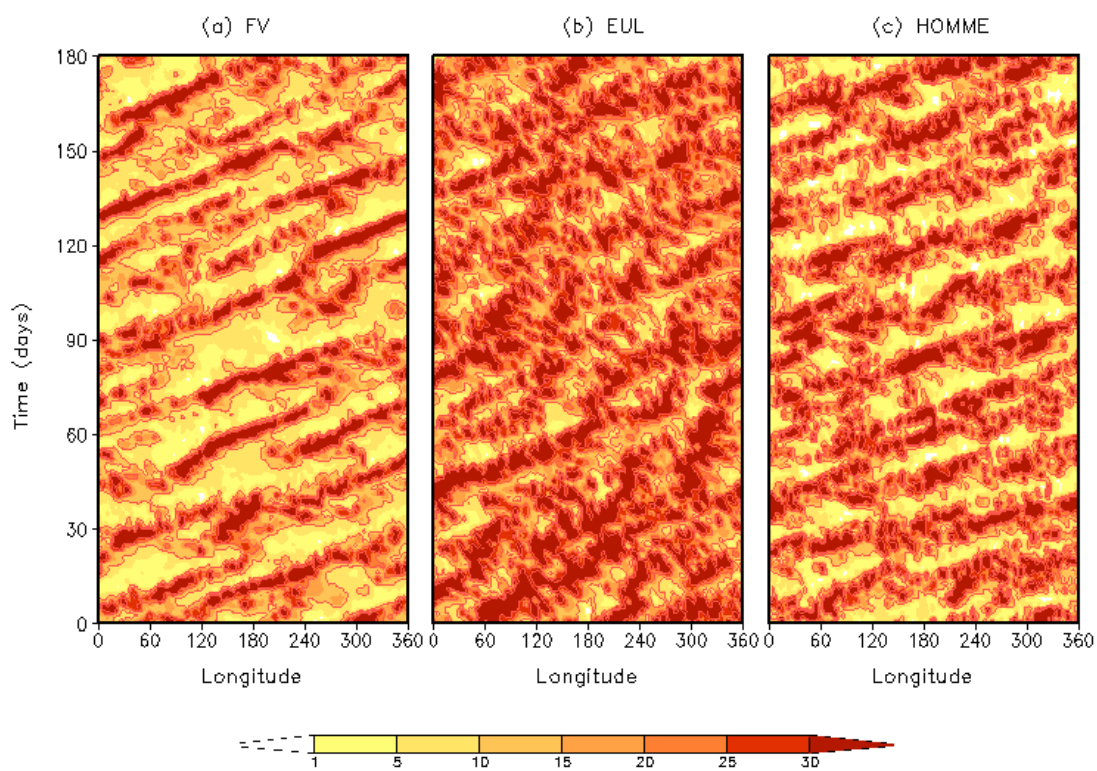


Figure 9: Longitude-Time diagrams of daily rainfall (mm/day) averaged between 2.5S - 2.5N from (a) FV, (b) EUL, and (c) HOMME.

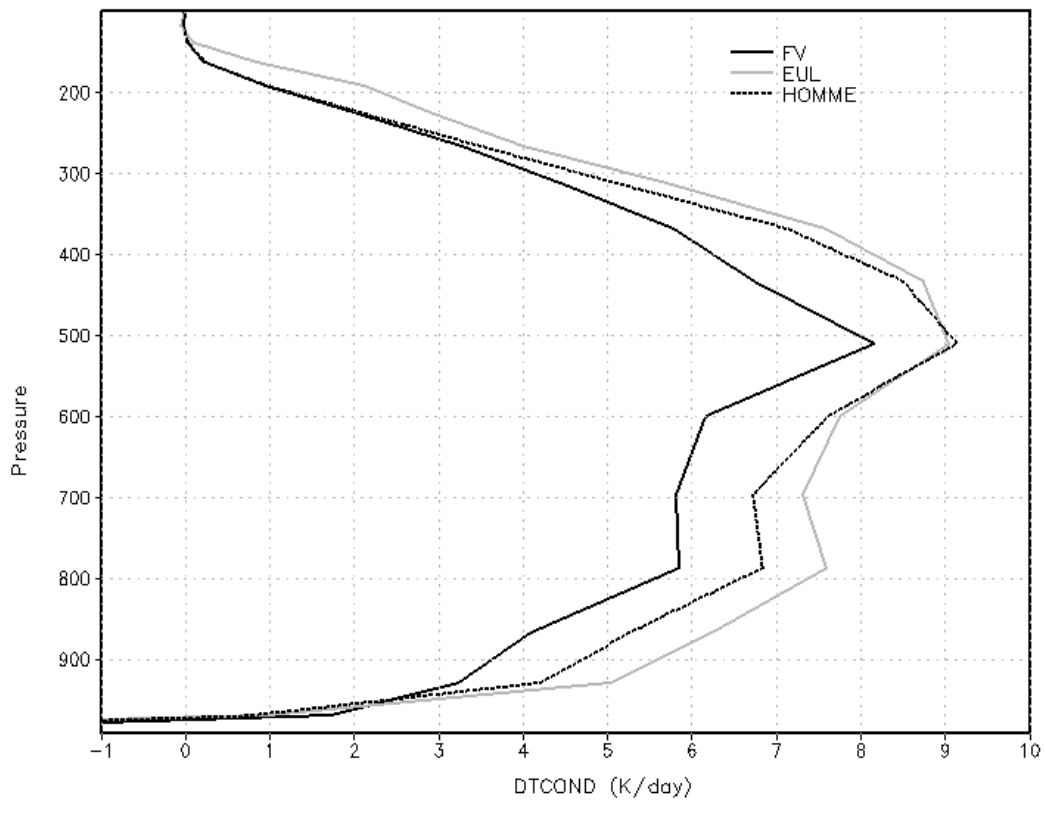


Figure 10: Vertical profile of the area averaged (0E to 360E and 2.5S to 2.5N) time mean moist heating from FV, EUL, and HOMME.

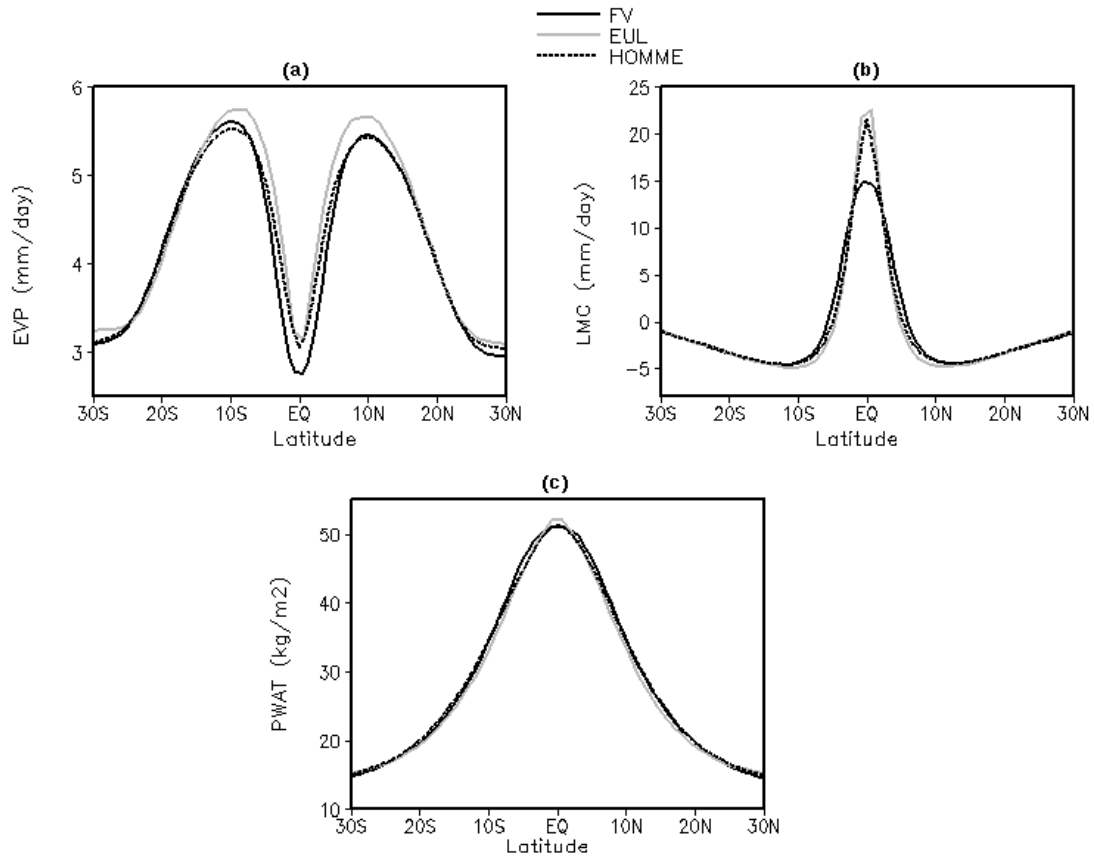


Figure 11: Zonally averaged time mean surface evaporation (mm/day), large-scale moisture convergence (mm/day), and precipitable water (kg/m²) from FV, EUL, and HOMME.

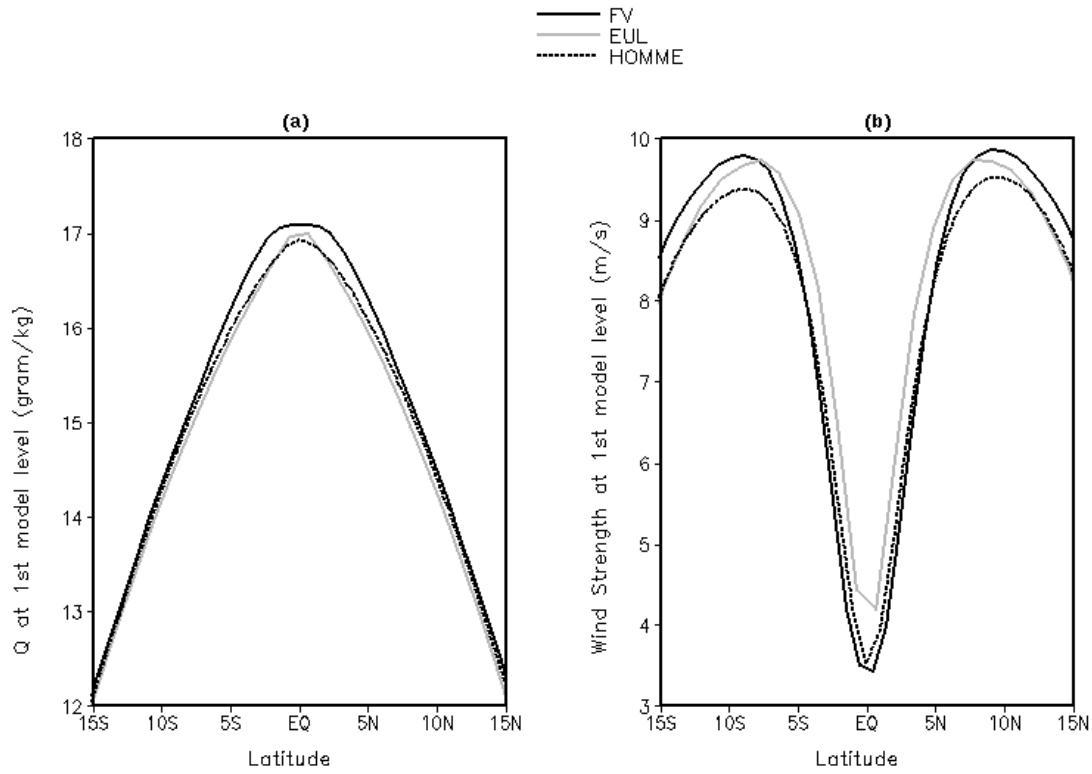


Figure 12: Zonally averaged time mean moisture deficit (gram/kg) and wind strength (m/s), at the 1st model level from FV, EUL, and HOMME.

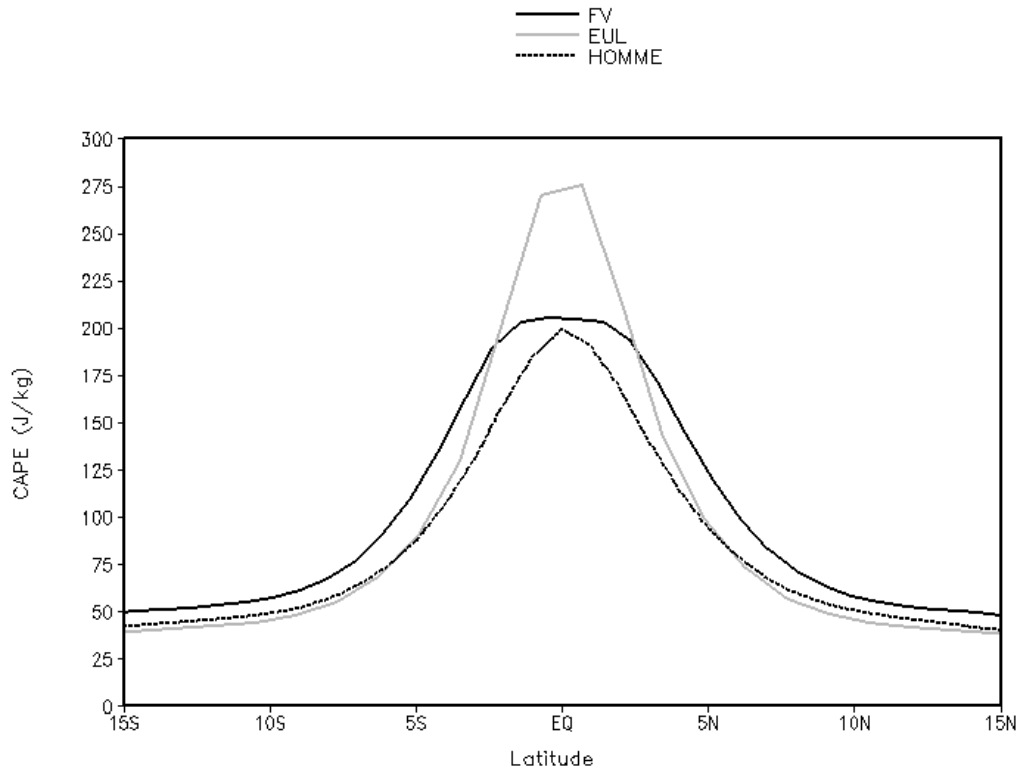


Figure 13: Zonally averaged time mean convective available potential energy (CAPE) from FV, EUL, and HOMME.

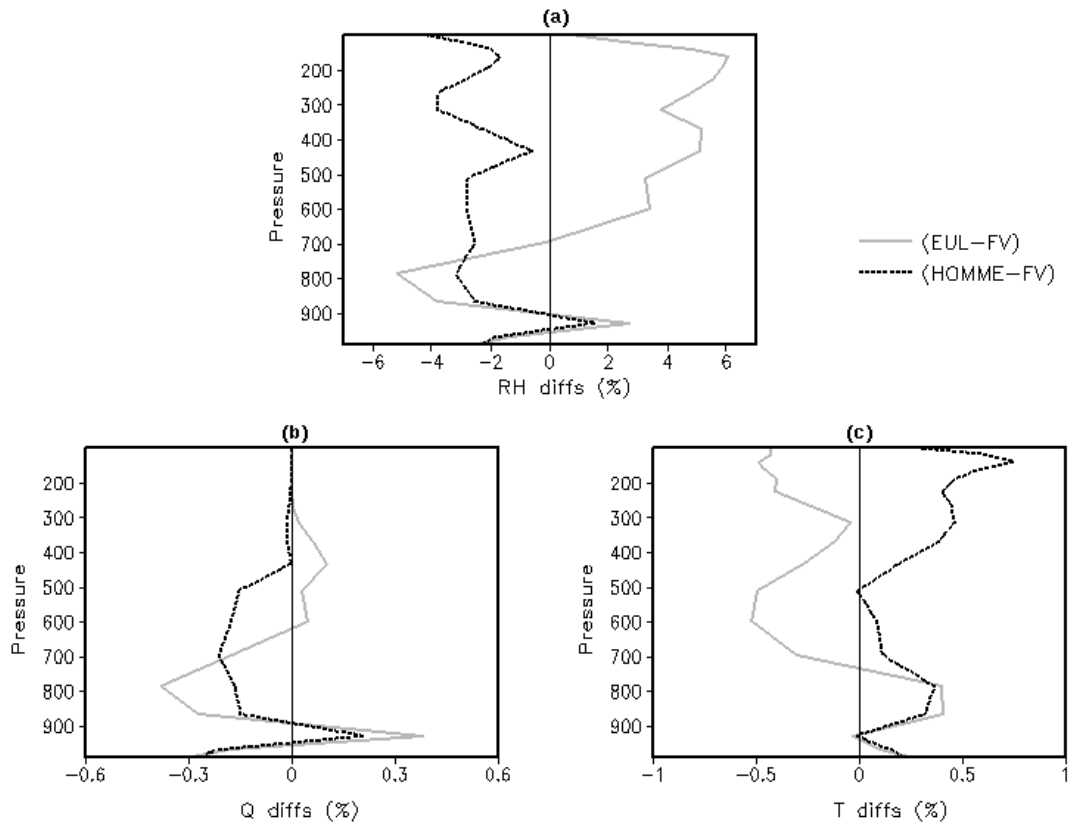


Figure 14: (a) Vertical profile of the area averaged (0E to 360E and 5S to 5N) time mean relative humidity for (EUL-FV) and (HOMME-FV). (b) Same as figure-a but for specific humidity. (c) Same as figure-a but for temperature. Notations used: RH for relative humidity, Q for specific humidity, and T for temperature.

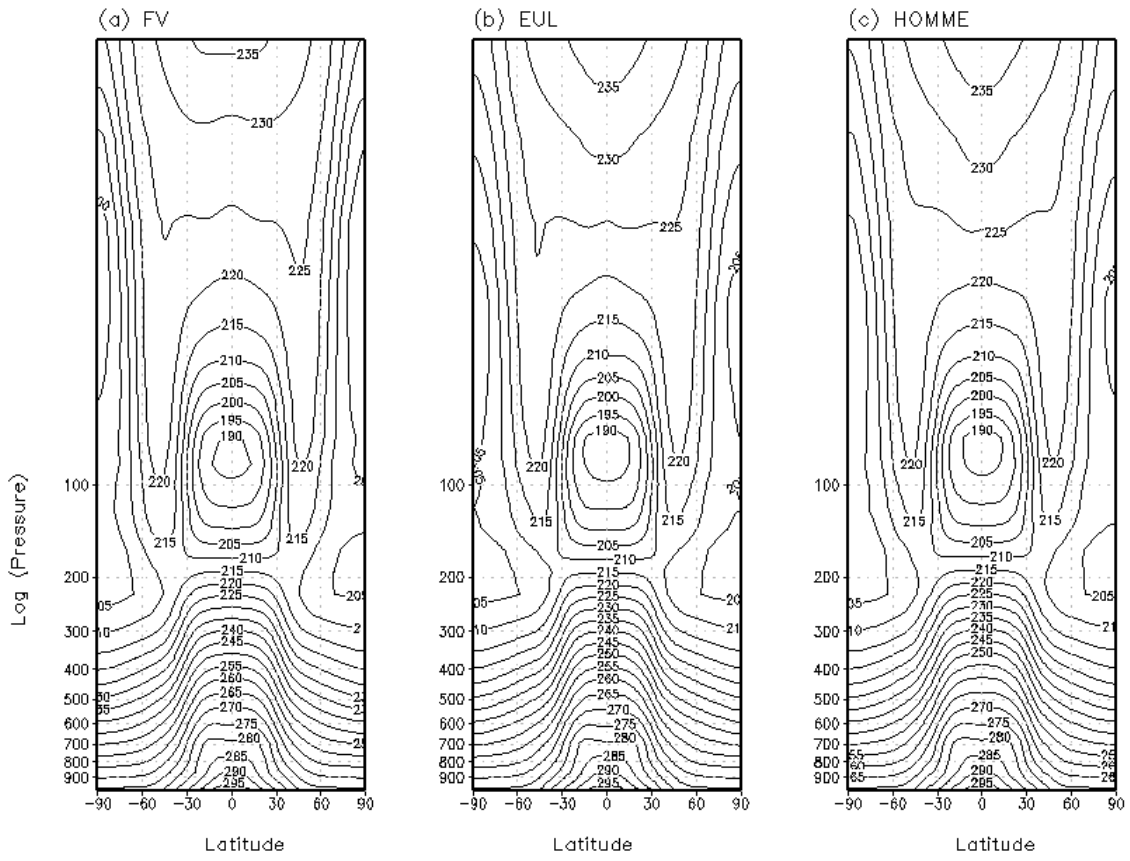


Figure 15: Zonally averaged time mean temperature (K) for (a) FV, (b) EUL, and (c) HOMME.

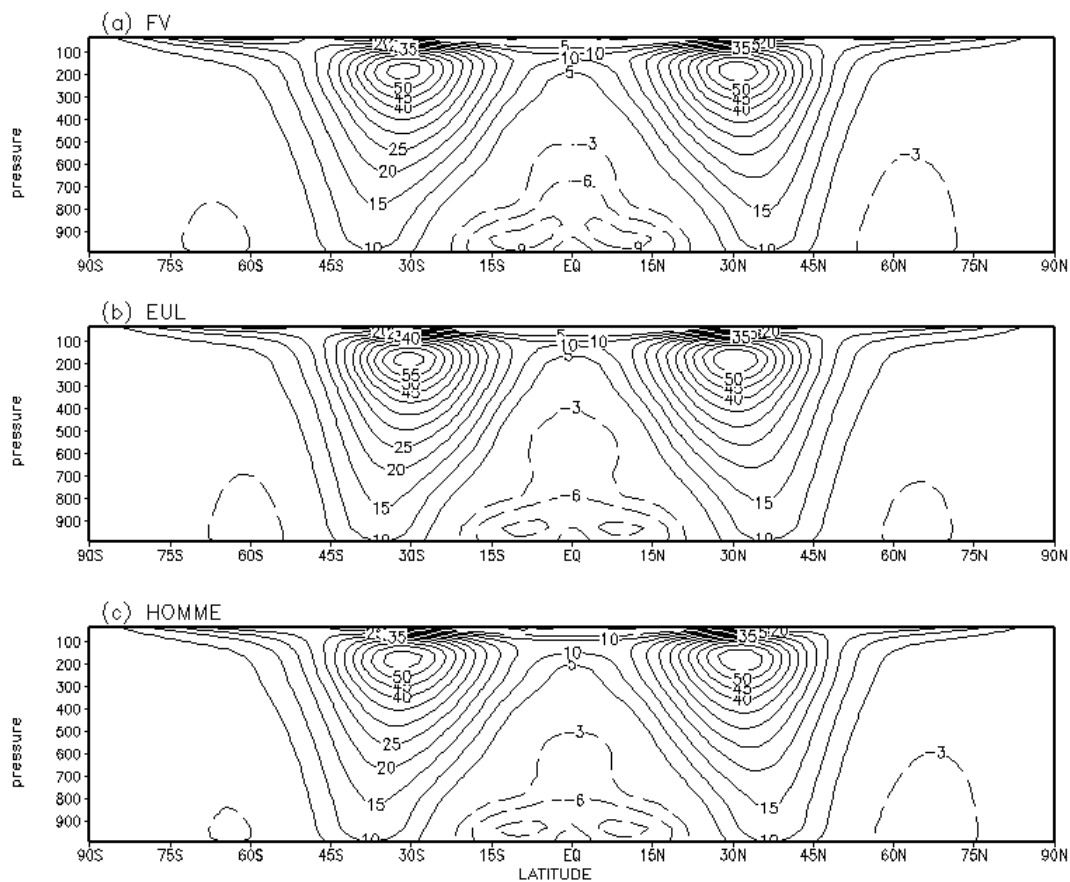


Figure 16: Zonally averaged time mean zonal wind (m/s) for (a) FV, (b) EUL, and (c) HOMME.

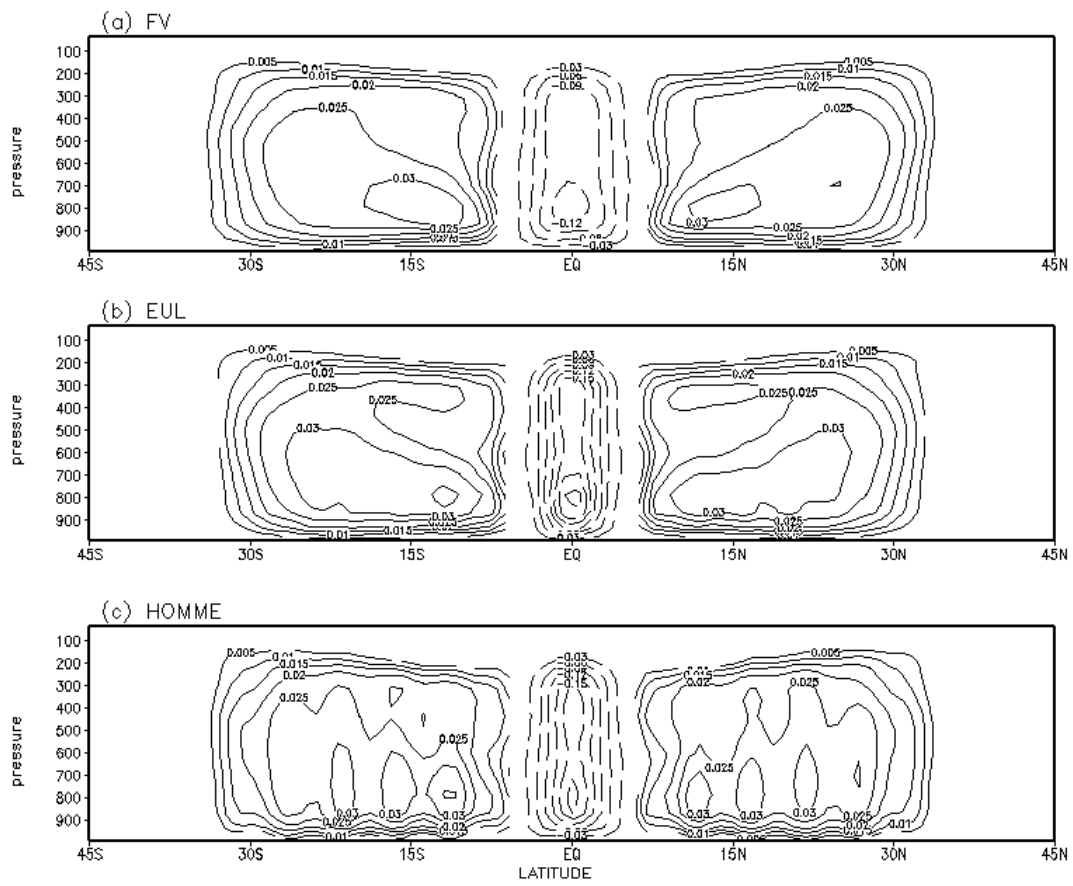


Figure 17: Zonally averaged time mean pressure vertical velocity (Pa/s) for (a) FV, (b) EUL, and (c) HOMME.

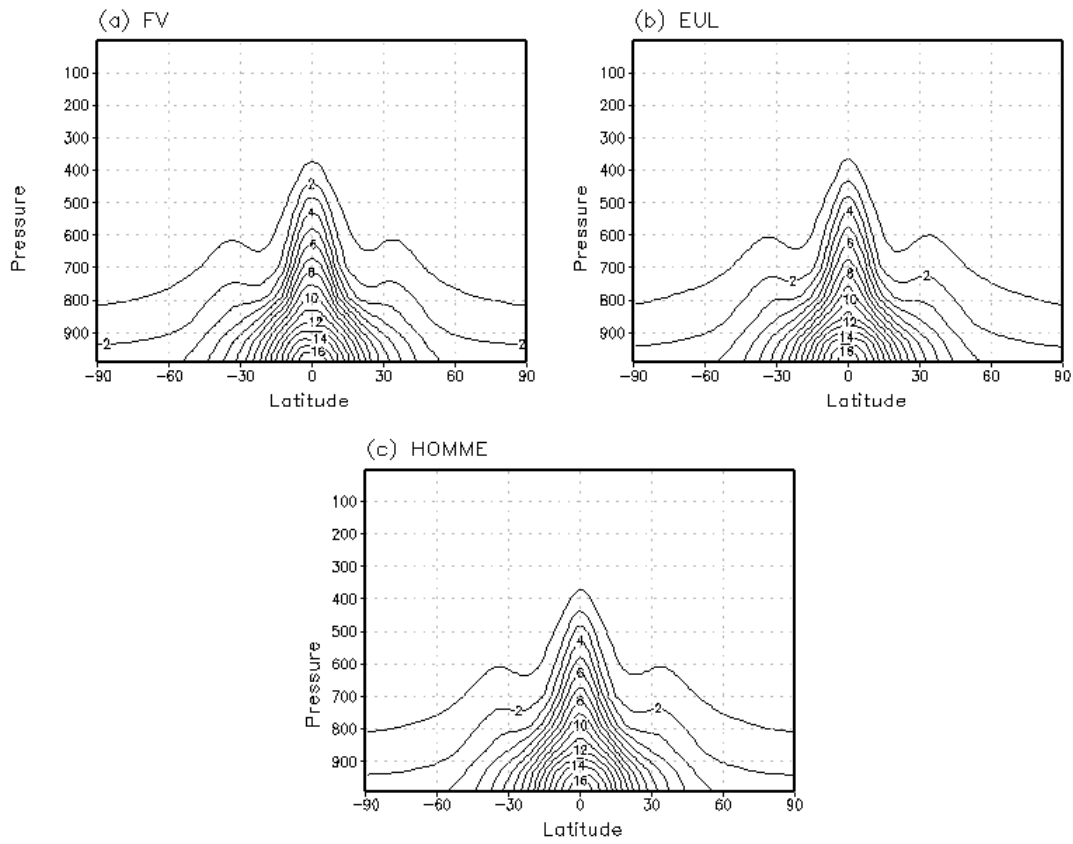


Figure 18: Zonally averaged time mean specific humidity (g/kg) for (a) FV, (b) EUL, and (c) HOMME.

Table

Dynamical Core	Global Mean TRF
FV	2.888
EUL	3.024
HOMME	2.948

Table 1. Global mean total rainfall (mm/day) from the three dynamical cores.